NANO LETTERS

Letter

pubs.acs.org/NanoLett

Subsurface Imaging of Coupled Carrier Transport in GaAs/AlGaAs Core–Shell Nanowires

Guannan Chen,[†] Terrence McGuckin,[†] Christopher J. Hawley,[†] Eric M. Gallo,[†] Paola Prete,[‡] Ilio Miccoli,[§] Nico Lovergine,[§] and Jonathan E. Spanier*[,†,∥]

[†]Department of Materials Science and Engineering and [∥]Department of Physics, Drexel University, 3141 Chestnut Street, Philadelphia, Pennsylvania 19104, United States

[‡]Istituto per la Microelettronica e Microsistemi (IMM), Consiglio Nazionale delle Ricerche (CNR), via Monteroni, 73100 Lecce, Italy

[§]Department of Innovation Engineering, University of Salento, via Monteroni, 73100 Lecce, Italy

Supporting Information

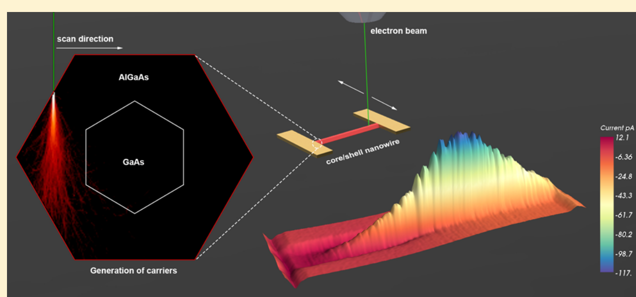

ABSTRACT: We demonstrate spatial probing of carrier transport within GaAs/AlGaAs core–shell nanowires with nanometer lateral resolution and subsurface sensitivity by energy-variable electron beam induced current imaging. Carrier drift that evolves with applied electric field is distinguished from a coupled drift-diffusion length. Along with simulation of injected electron trajectories, combining beam energy tuning with precise positioning for selective probing of core and shell reveals axial position- and bias-dependent differences in carrier type and transport along parallel conduction channels. These results indicate how analysis of transport within heterostructured nanomaterials is no longer limited to nonlocal or surface measurements.

KEYWORDS: *Electron beam induced current (EBIC), subsurface imaging, scanning probe microscopy, heterostructured nanowire, core–shell nanowire*

Light–matter interactions in semiconductor nanowires are drivers of new optoelectronic and photonic devices.[1−5] In III–V semiconductor heterostructures, the interface forms the basis for high-speed devices from band engineering and modulated doping.[6,7] For instance, Type I heterostructures[8] such as GaAs–AlGaAs are beneficial for confinement of carriers and for transferred electron phenomena.[9,10] Heterostructures in coaxial core–shell nanowires permit the study of how finite size, shape, strain, interfacial atomic structure, defects, and surface influence electrostatic potential landscape and carrier conduction paths, thereby enabling new nanoelectronic device paradigms.[11−13] In buried heterostructures such as a core with one or more surrounding shells, however, local information about excess carrier transport within and between each component needed to understand device functionality is not readily available. Additionally, increased surface-to-volume ratio in a nanowire is accompanied by surface traps, band bending, and surface recombination, all of which affect intrinsic electronic properties.[14−16] Despite remarkable advances,[17,18] understanding of coupling of carrier transport within core–shell nanowire components remains lacking. Thus, local probing of nanoscale contributions from carriers within surface and subsurface nanostructured components under device operating conditions brings new insight into the operation and design of nanoscale heterojunction-based devices.

Spatially resolved current mapping with local injection of excess carriers, e.g., electron beam induced current (EBIC) and scanning photocurrent (SPC), yields characteristic lengths such as the depletion width at a Schottky contact,[19] diffusion length at a p–n junction or within a homogeneous material,[20] and defect-induced band bending.[21] Effective in studying excess carrier transport dynamics[22] at the interface of a semiconductor heterostructure, EBIC has superior lateral spatial resolution compared to optical diffraction-limited SPC. While a submicron carrier transport channel in nanowire devices is typical especially for ballistic transport studies,[23] imaging along the NW radial direction demands much finer resolution: this can, in principle, be addressed by EBIC where ultimate resolution is limited by a combination of factors. Among these are electron optics and beam stability, carrier trajectory and electron beam energy- and material-dependent interaction profile, beam sweep rate and signal-to-noise, and drift.

Taking advantage of the large penetration depth of an electron beam, we demonstrate a highly versatile subsurface functional imaging approach by combining the selection of different beam energy regimes in EBIC mapping with Monte Carlo simulations of scattering of injected electrons and their

Received: August 4, 2014
Revised: November 10, 2014
Published: December 29, 2014

© 2014 American Chemical Society

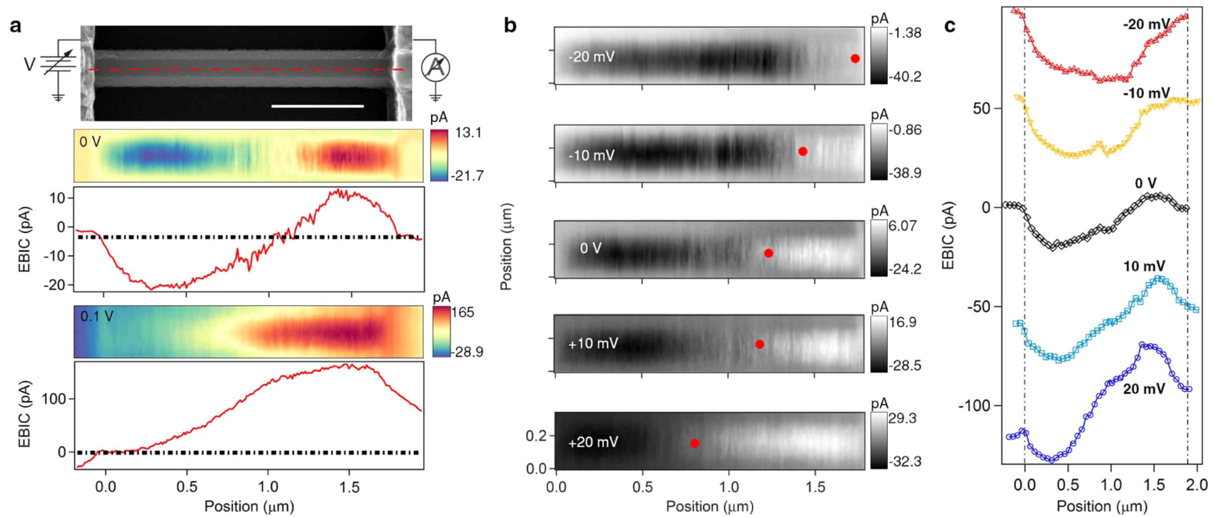

Figure 1. Evolution of the electronic landscape at the onset of small bias voltage. (a) EBIC images and selected line profiles V_b = 0 V (middle) and V_b = 0.1 V (bottom) taken along the center axis of the nanowire (red dash−dot line in SEM image). The right side contact is grounded. The black dash−dot lines denote zero current. The scale bar is 500 nm. A circuit diagram is superimposed on the SEM image to indicate the bias direction. (b) Series of EBIC images collected −20 mV < V_b < +20 mV. Red dots indicate the location along the nanowire where the sign of the current changes. (c) The EBIC central axis line profiles extracted from (b). Profiles are offset by 50 pA for clarity.

trajectories. In a GaAs−AlGaAs core−shell nanowire, for example, the beam interacts mainly with the surrounding shell at low accelerating voltage (V_{acc} < 3 kV), whereas for V_{acc} > 5 kV the contribution from the core is apparent, even dominant. When a higher energy beam is used, a large penetration depth is accompanied by a expansion of beam interaction area deep under the surface due to beam electron trajectory from the scattering events. However, we found from the trajectory simulation results that a lateral resolution of ≈10 nm can be achieved.

To avoid complication from effects due to electrical contacts,[24] devices were prepared with Ohmic contacts on the ends of each nanowire core (Methods and Supporting Information). A field-effect hole mobility of 13 cm^2 V^{-1} s^{-1} is estimated from back-gate results.[25,26] The value is expected to be lower than the intrinsic core mobility due to the shielding effect from the shell and insufficient coupling and inhomogeneous field.[26,27]

For low V_{acc} (= 3 kV) and at zero bias V_b (Figure 1), the signal profile along the axis of the nanowire is antisymmetric due to diffusion and local injection-induced field, an effect that is not intuitive, but has been successfully modeled numerically.[28] The central antisymmetric point corresponds to a net zero current from the equal number of carriers diffusing to either contact. When the injection point moves away from the center (e.g., to the right), the induced field compensates the faster electron diffusion, and a net positive current is reached in the steady state. From 0 < V_b < 0.1 V, the EBIC axial line profiles reveal a remarkable transition from antisymmetric, in which the diffusion and injection induced field dominate the transport, to a peak shape with the same sign of excess current and having nearly exponential decay on both sides (Figure 1a). It is due to the fact that the external electric field (even at 0.1 V) is sufficiently large to overwhelm the effect from injection induced field. We investigated the process of this transition more closely. By increasing V_b from negative to positive in the vicinity of zero-bias (Figure 1b), a continuous shift of the antisymmetric point (≈1.2 μm over 40 mV) is evident. At even higher positive (negative) bias, the negative (positive) part of the signal is merged into the corresponding contact, and the entire profile evolves into having a unidirectional sign.

By introducing a larger uniform external electric field along the length of the nanowire, the signal is significantly enhanced due to the drift current component. The two mechanisms of transport, diffusion and drift, form a self-consistent carrier propagation pattern characterized by a joint decay length. A peak appears indicating a transition from electron- to hole-limited current. By moving the injection point away from the peak, the number of excess carriers reaching their respective collecting electrode decays exponentially. The sign of the current over the entire nanowire is unidirectional. The contribution of drift component becomes more significant at higher bias. Serial EBIC scans at biases ranging from 1 to 5 V with the interval of 1 V are shown in Figure 2. When the bias is increased, the peak shifts toward the carrier collector for which the corresponding type of carrier has lower mobility. At V_{acc} = 5 kV, the beam mainly interacts with the shell. The peak shift is not significant since AlGaAs has a low electron mobility and the mobility difference between electrons and holes is minor. When the bias increases from 0.1 to 0.5 V, the electron decay length obtained by exponential fitting evolves from 0.60 to 1.05 μm and the hole decay length from 0.31 to 0.68 μm (Figure 2a, c). The extracted lengths are also typical for $Al_{0.24}Ga_{0.76}As$.[29] Under bias, the decay lengths are altered from the symmetric diffusion of carriers from a point injection, those along the applied field extended and against the field shortened. A more quantitative approach can be understood from the diffusion-drift continuity equation with the drift term associated with mobility and electric field[30] (Supporting Information). The derived drift component can be expressed as $L_{drift,n} = L_1 - L_{diff,n}^2/L_1$ where drift length is introduced as $L_{drift,n} = \mu_n \tau_n E$, with μ_n and τ_n the mobility and lifetime of electrons, respectively, and E the electric field. L_1 is the measured decay length, and $L_{diff,n}$ denotes pure diffusion length at zero bias.

The drift components derived from the extracted decay lengths are found to be linearly dependent on the applied field. From the drift component, important transport parameters are uncovered. Our result gives a $\mu\tau$ product of 2.78 × 10^{-8} cm^2

DOI: 10.1021/nl502995q
Nano Lett. 2015, 15, 75−79

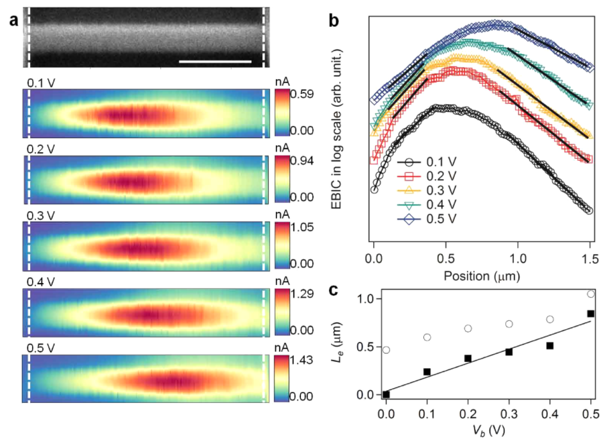

Figure 2. EBIC at low accelerating voltage V_{acc}. (a) EBIC maps of a single NW device at V_b = 0.1, 0.2, 0.3, 0.4, and 0.5 V (right side contact is grounded). White dashed lines indicate the locations of the contacts. The secondary electron image (top) is collected simultaneously, and the scale bar is 500 nm. (b) Line profiles along NW axial direction. Best fittings are shown in solid lines (black) on both sides of the EBIC signal maxima. (c) Electron drift component (solid squares) is separated from the diffusion-drift decay length (open circles); both are plotted versus V_b. The line in (c) is a linear fit of the drift length vs V_b.

V^{-1} for electrons in the shell. An electron lifetime of ≈2 ns is expected,[16] and thus the mobility is estimated to be ≈10 cm^2 V^{-1} s^{-1}. The value is lower than bulk value probably due to a moderate doping and surface depletion. Considering the additional contribution from the GaAs core at high bias, the actual value may be even lower. Indeed, a small fraction of injected electrons penetrates deep enough to reach the high-mobility GaAs core. A shift in the peak position toward the hole collector is observed for V_b > 0.4 V when the core drift current component becomes large enough. The phenomenon is more conspicuous for larger beam energies.

Progressively larger accelerating voltages, coupled with nanometer-scale lateral resolution, enable high selectivity in subsurface nanostructure component transport characteristics. For example, with V_{acc} = 10 kV, the interaction volume reaches the GaAs core (Figure 3c), where the signal has contributions from both the core and the shell (Figure 3a). The integration of the Monte Carlo-simulated carrier density generated by the incident electron beam over different regions (i.e., core and shell) enables construction of spatial profiles and differences in generation rates along the nanowire radius within the core and shell (Figure 3d, Methods and Supporting Information). Compared with V_{acc} = 3 or 5 kV, the generated carrier density in the core when beam position is at the center for V_{acc} = 10 kV is comparable to that in the shell due to larger penetration depth. Indeed, the central profile involves both the core and shell. Since the core electron mobility is expected to be significantly higher, the average joint decay length is expected to increase as a result. A direct comparison is shown in Figure 3b between scans under a 5 kV beam and a 10 kV beam at V_b = 0.5 V. A clear increase of decay length at 10 kV is seen. In fact, such an increase occurs in the entire bias range from 0.1 to 0.5 V (Figure 3b, inset). This difference without ambiguity demonstrates that a high-mobility core contributes to the overall EBIC with a dominating drift current component.

Striking differences in the EBIC profiles collected along the nanowire axis at center and at side (the Monte Carlo is shown in Figure S2b) reveal the effects of different carrier properties in the core and shell, respectively (Figure 3e). For the center profile where the e-beam interacts with both the core and the shell, shifts in the location of the observed peak with different bias are opposite that for the side profile, where only the shell is concerned. Again, the direction of EBIC peak shift depends on the mobility difference. When V_b > 0.2 V the opposite direction of peak shift between the central and side profiles is observed due to the dominance of the core contribution at larger bias. For the core, the shift is toward the hole collecting electrode

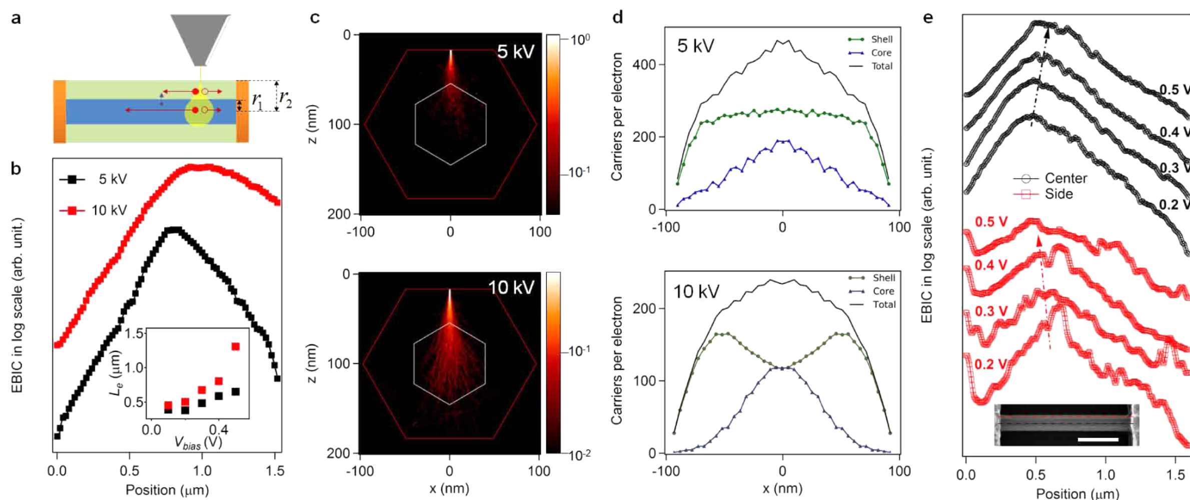

Figure 3. Beam energy-selective EBIC revealing transport in GaAs core. (a) Illustration of beam interaction with the two parallel transport channels having different excess carrier transport properties. The different length of red arrows indicates the mobility difference, and the purple arrow indicates the possible interaction between the core and the shell. (b) Comparison of the EBIC line profiles under V_{acc} = 5 kV (black) and V_{acc} =10 kV (red) at V_b = 0.5 V. The inset shows evolution of the decay lengths versus V_b for V_{acc} = 5 kV (black squares) and V_{acc} = 10 kV (red squares). Monte Carlo simulations of (c) beam trajectories when the beam is on the central NW axis and (d) carrier generation dependence on beam incident positions obtained by integrating in core and shell areas in maps, for (c) in $GaAs/Al_{0.24}Ga_{0.76}As$ nanowire cross sections with hexagonal facets, under two different values of V_{acc}. (e) EBIC profiles at central axis (black) and side axis in shell region (red) as denoted in the inset (scale bar is 500 nm), revealing opposite drift directions.

DOI: 10.1021/nl502995q
Nano Lett. 2015, 15, 75−79

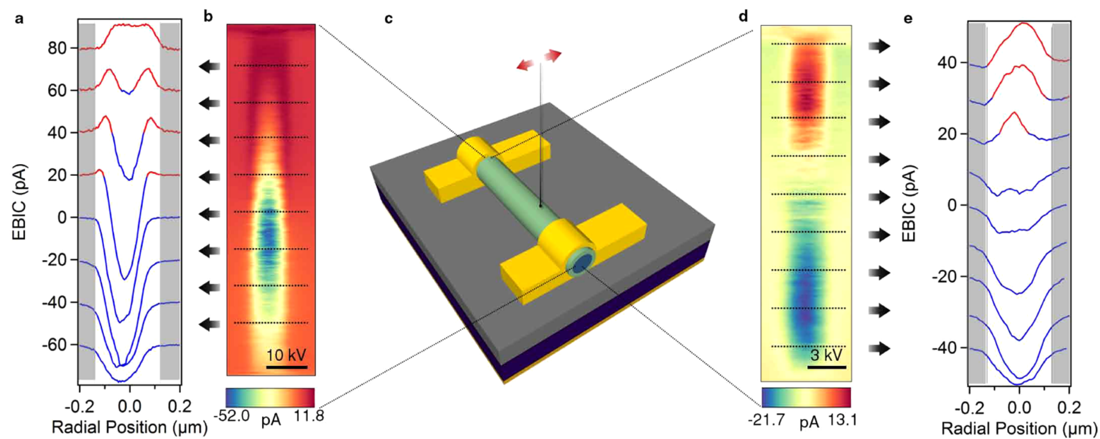

Figure 4. High-resolution radial profiles at zero bias. (a and e) Radial line profiles extracted at 200 nm intervals with V_{acc} = 10 kV and V_{acc} = 3 kV from EBIC maps (b) and (d), respectively, where black dashed lines denote the corresponding axial locations from which profiles in (a) and (e) have been extracted in an electrically interfaced nanowire as illustrated in (c). Radial line profiles presented in (a) and (e) have two colors: red indicates positive current and blue negative. Gray areas in (a) and (e) denote areas exterior to the nanowire. Radial current profiles are offset by 20 pA in (a) and 10 pA in (e) for clarity.

due to electron having a larger mobility, whereas the shell shows a shift, though not as significant, to the electron collecting electrode. Considering the radial distance between where the two profiles are extracted, these results explicitly demonstrate that transport characteristics near a subsurface heterostructure can be resolved to within ≈10 nm in the imaging plane.

Radial profiles collected using different V_{acc} reveal carrier and transport types and the degree of coupling between core and shell channels. Extraction of a series of radial profiles collected using V_{acc} = 3 and 10 kV at zero bias along different axial positions reveals changes in the sign of the current in several profiles (Figure 4). Distinct parallel transport channels from the core and the shell can be discerned at 10 kV. Significantly, current sign inversion from core to shell within a radial scan at the same axial channel position further indicates carrier transport in the two channels is partially decoupled (i.e., the core and shell channels possess their respective zero-bias profiles while the interaction between channels is negligible). Unlike carriers with different properties in homogeneous material tending to form a self-consistent ambipolar coefficient, the energy barrier at the core–shell interface impedes the interaction between two individual transport channels. When the beam interacts only with the shell (Figure 4b) the difference in the current profiles is limited to only amplitude since the decay length is expected to be uniform in homogeneous material. The EBIC scan in Figure 4d is identical to Figure 1a. We note that the hole is also subject to the band bending which may facilitate a transfer of the holes in the shell across the interface into the core. However, the shell holes have both a short recombination time and low mobility resulting in an insignificant contribution to the overall current. Additionally, the surface depletion induced band bending drives the hole to the reverse direction. Therefore, such effect is negligible in the EBIC signal especially when the core and shell have similar values of hole mobilities. Finally, we also note that, if axial profiles are extracted from Figure 4d, the antisymmetric point (zero current) for the profiles on the shell portion (the side regions) at the axial center point are consistent with those of 3 kV, both of which consist of the signal from the shell section only. The fact that the zero current point in the core region is not at the axial center of the NW is due to a difference in the contact resistance on the core that arises inherently from the annealing process.

In summary, we have spatially resolved carrier transport in a core–shell heterostructure nanowire with unprecedented high resolution and capability of subsurface probing by energy variable EBIC. The coupling of unprecedentedly fine lateral resolution in current imaging with electron energy-based depth, guided by simulated electron trajectories, now opens the possibility of simultaneous nanoscale discrimination of carrier type and dominant transport mechanism selectively within different media in heterogeneous nanoscale electronic devices.

Methods. *Nanowire Growth and Device Preparation.* GaAs/$Al_{0.24}Ga_{0.76}As$ NWs used in this study are grown by Au-nanoparticle-catalyzed metalorganic vapor phase epitaxy (Aixtron) on 111(B)-terminated GaAs substrates. The growth of GaAs NW cores having diameters of 60 nm was carried out using $(CH_3)_3Ga$ and $(C_4H_9)AsH_2$ as metal–organic precursors at a growth temperature of 400 °C, and AlGaAs shells with thickness ranging around 70 nm were subsequently grown at 650 °C with the addition of $(CH_3)_3Al$. Low-temperature photoluminescence (PL) is used to estimate the Al percentage from shell band edge excitonic emission as previously reported.[31] The GaAs core is lightly *p*-typed unintentionally doped with carbon from the precursors. The AlGaAs shell is *n*-typed doped with Si. With an overall nanowire diameter ≈200 nm, a SiO_2/Si substrate, and a moderate beam current of only 100 pA, the thermoelectric current by local heating from Seebeck effect is negligible and therefore excluded from the analysis.[32] We used a multilayer e-beam metal evaporation consisting of Pd, Zn, Ti, and Au for Ohmic contract formation. The out-diffusion of Ga in the nanowire through Pd, activated by a rapid thermal annealing at 400 °C, leaves vacancies for Zn to occupy and to form local doping under the contact area, which promotes carrier tunneling and reduces the contact resistance. The devices are defined with e-beam lithography (NPGS, Bozemann, MT), and the metallization process is conducted in e-gun evaporator (BOC Edwards). All devices are subject to gentle oxygen plasma cleaning for 5–15 min before measurement inside a field-emission scanning electron micro-scope (FEI DB235, Hillsboro OR) chamber to avoid residual carbon deposition in the vicinity of the beam.

DOI: 10.1021/nl502995q
Nano Lett. 2015, 15, 75–79

Electron Beam Induced Current. Measurements were conducted with a custom-built low-noise EBIC system (Mighty EBIC, Ephemeron Laboratories, Philadelphia PA and Drexel University) installed on a scanning electron microscope (FEI DB235). A transimpedance amplifier was used to convert the current signal into a voltage. All measurements were done in a DC configuration. The substrate was held at ground, the beam current for all acceleration voltages used was ≈100 pA, and the dwell time at each pixel before measuring the signal was 0.5 ms.

Spatial Drift and Vibrational Noise Correction. To enable longer scan times for increased resolution, an algorithm was developed and implemented to remove drift and vibrational noise from the images. The procedure locates the center of the nanowire along the axial direction using the secondary electron image as a reference and computes the gradient for each line of the scan. The center is defined as the average of the positions of maximum and minimum values of the gradient. The data points are extracted around the center and repositioned.

Monte Carlo Simulations. Electron flight paths through the GaAs-core, AlGaAs-shell nanowire were simulated using Casino3.2.[33] The simulation space was 200 nm × 200 nm × 100 nm with a grid spacing of 1 nm. The incident beam was scanned radially along the nanowire in 5 nm increments at beam energies of 3, 5, and 10 kV. The number of carriers generated was estimated in the core and shell by dividing the energy lost at each point by $3E_g$ of GaAs and AlGaAs at 300 K.

■ ASSOCIATED CONTENT

Supporting Information

Description of experimental and simulation results: Ohmic contact on low-doping GaAs; supplementary Monte Carlo simulation results; model for drift-diffusion coupling; derivation of drift component; and cited references. This material is available free of charge via the Internet at http://pubs.acs.org.

■ AUTHOR INFORMATION

Corresponding Author

*E-mail: spanier@drexel.edu.

Author Contributions

G.C. and T.M. contributed equally to this work.

Notes

The authors declare no competing financial interest.

■ ACKNOWLEDGMENTS

Work at Drexel University was supported by the National Science Foundation under DMR 0907381 and DMR 1124696 and by the Nanoscale Research Initiative of the Semiconductor Research Corporation. The authors also acknowledge NSF DMR 0722845 and the Drexel University Centralized Research Facilities for acquisition of and access to instrumentation, respectively. T.M. and C.J.H. were supported by the US Dept. of Education GAANN-RETAIN program (P200A100117), and E.M.G. was supported by a NSF Graduate Research Fellowship.

■ REFERENCES

(1) Tomioka, K.; Yoshimura, M.; Fukui, T. *Nature* **2012**, *488*, 0–4.

(2) Pribiag, V. S.; Nadj-Perge, S.; Frolov, S. M.; van den Berg, J. W. G.; van Weperen, I.; Plissard, S. R.; Bakkers, E. P. A. M.; Kouwenhoven, L. P. *Nat. Nanotechnol.* **2013**, *8*, 170–174.

(3) Cao, L.; Nabet, B.; Spanier, J. E. *Phys. Rev. Lett.* **2006**, *96*, 157402.

(4) Cao, L.; White, J. S.; Park, J.-S.; Schuller, J. A.; Clemens, B. M.; Brongersma, M. L. *Nat. Mater.* **2009**, *8*, 643–647.

(5) Kelzenberg, M. D.; Boettcher, S. W.; Petykiewicz, J. A.; Turner-Evans, D. B.; Putnam, M. C.; Warren, E. L.; Spurgeon, J. M.; Briggs, R. M.; Lewis, N. S.; Atwater, H. A. *Nat. Mater.* **2010**, *9*, 239–244.

(6) Mani, R. G.; Smet, J. H.; von Klitzing, K.; Narayanamurti, V.; Johnson, W. B.; Umansky, V. *Nature* **2002**, *420*, 646–50.

(7) Walker, R. *IEEE J. Quantum Electron.* **1991**, *27*, 654–667.

(8) Adachi, S. *J. Appl. Phys.* **1985**, *58*, R1.

(9) Hess, K.; Morkoç̀ğ, H.; Shichijo, H.; Streetman, B. G. *Appl. Phys. Lett.* **1979**, *35*, 469.

(10) Chen, G.; Gallo, E.; Leaffer, O.; McGuckin, T.; Prete, P.; Lovergine, N.; Spanier, J. *Phys. Rev. Lett.* **2011**, *107*, 1–5.

(11) Dick, K. A.; Caroff, P.; Bolinsson, J.; Messing, M. E.; Johansson, J.; Deppert, K.; Wallenberg, L. R.; Samuelson, L. *Semicond. Sci. Technol.* **2010**, *25*, 024009.

(12) Krogstrup, P.; Popovitz-Biro, R.; Johnson, E.; Madsen, M. H.; Nygå rd, J.; Shtrikman, H. *Nano Lett.* **2010**, *10*, 4475–82.

(13) Chen, G.; Sun, G.; Ding, Y. J.; Prete, P.; Miccoli, I.; Lovergine, N.; Shtrikman, H.; Kung, P.; Livneh, T.; Spanier, J. E. *Nano Lett.* **2013**, *13*, 4152–4157.

(14) Thunich, S.; Prechtel, L.; Spirkoska, D.; Abstreiter, G.; Fontcuberta i Morral, A.; Holleitner, A. W. *Appl. Phys. Lett.* **2009**, *95*, 083111.

(15) Gallo, E. M.; Chen, G.; Currie, M.; McGuckin, T.; Prete, P.; Lovergine, N.; Nabet, B.; Spanier, J. E. *Appl. Phys. Lett.* **2011**, *98*, 241113.

(16) Demichel, O.; Heiss, M.; Bleuse, J.; Mariette, H.; Fontcuberta i Morral, A. *Appl. Phys. Lett.* **2010**, *97*, 201907.

(17) Storm, K.; Halvardsson, F.; Heurlin, M.; Lindgren, D.; Gustafsson, A.; Wu, P. M.; Monemar, B.; Samuelson, L. *Nat. Nanotechnol.* **2012**, *7*, 718–722.

(18) Montazeri, M.; Jackson, H. E.; Smith, L. M.; Yarrison-Rice, J. M.; Kang, J.-H.; Gao, Q.; Tan, H. H.; Jagadish, C. *Nano Lett.* **2012**, *12*, 5389–95.

(19) Gu, Y.; Kwak, E.-S.; Lensch, J. L.; Allen, J. E.; Odom, T. W.; Lauhon, L. J. *Appl. Phys. Lett.* **2005**, *87*, 043111–3.

(20) Gutsche, C.; Niepelt, R.; Gnauck, M.; Lysov, A.; Prost, W.; Ronning, C.; Tegude, F.-J. *Nano Lett.* **2012**, *12*, 1453–8.

(21) Kittler, M.; Ulhaq-Bouillet, C.; Higgs, V. *J. Appl. Phys.* **1995**, *78*, 4573.

(22) Eisenbeiss, A.; Heinrich, H.; Opschoor, J.; Tijburg, R. P.; Preier, H. *Appl. Phys. Lett.* **1987**, *50*, 1583–1585.

(23) Xiang, J.; Lu, W.; Hu, Y.; Wu, Y.; Yan, H.; Lieber, C. M. *Nature* **2006**, *441*, 489–93.

(24) Ahn, Y.; Dunning, J.; Park, J. *Nano Lett.* **2005**, *5*, 1367–1370.

(25) Wunnicke, O. *Appl. Phys. Lett.* **2006**, *89*, 083102.

(26) Khanal, D. R.; Wu, J. *Nano Lett.* **2007**, *7*, 2778–2783.

(27) Storm, K.; Nylund, G.; Samuelson, L.; Micolich, A. P. *Nano Lett.* **2012**, *12*, 1–6.

(28) Fu, D.; Zou, J.; Wang, K.; Zhang, R.; Yu, D.; Wu, J. *Nano Lett.* **2011**, *11*, 3809–15.

(29) Zarem, H. A.; Sercel, P. C.; Lebens, J. A.; Eng, L. E.; Yariv, A.; Vahala, K. J. *Appl. Phys. Lett.* **1989**, *55*, 1647.

(30) Ferry, D. *Semiconductor Transport*; Taylor & Francis: London, 2000; p 384.

(31) Prete, P.; Marzo, F.; Paiano, P.; Lovergine, N.; Salviati, G.; Lazzarini, L.; Sekiguchi, T. *J. Cryst. Growth* **2008**, *310*, 5114–5118.

(32) Prechtel, L.; Padilla, M.; Erhard, N.; Karl, H.; Abstreiter, G.; Fontcuberta i Morral, A.; Holleitner, A. W. *Nano Lett.* **2012**, 2337–2341.

(33) Demers, H.; Poirier-Demers, N.; Couture, A. R.; Joly, D.; Guilmain, M.; de Jonge, N.; Drouin, D. *Scanning* **2011**, *33*, 135–146.

DOI: 10.1021/nl502995q
Nano Lett. 2015, 15, 75–79